CrossMark

Laboratory and numerical experiments on the near wake of a sphere in a stably stratified ambient

T.J. Madison[1], X. Xiang[1] and G.R. Spedding[1],†

[1]Department of Aerospace and Mechanical Engineering, University of Southern California, Los Angeles, CA 90081, USA

The flow around and behind a sphere in a linear density gradient has served as a model problem for both body-generated wakes in atmospheres and oceans, and as a means of generating a patch of turbulence that then decays in a stratified ambient. Here, experiments and numerical simulations are conducted for 20 values of Reynolds number, *Re*, and internal Froude number, *Fr*, where each is varied independently. In all cases, the early wake is affected by the background density gradient, notably in the form of the body-generated lee waves. Mean and fluctuating quantities do not reach similar states, and their subsequent evolution would not be collapsible under any universal scaling. There are five distinguishable flow regimes, which mostly overlap with previous literature based on qualitative visualisations and, in this parameter space, they maintain their distinguishing features up to and including buoyancy times of 20. The possible relation of the low {*Re*, *Fr*} flows to their higher {*Re*, *Fr*} counterparts is discussed.

Key words: stratified flows

1. Introduction

1.1. *The sphere wake as a model problem*

The evolution of a sphere wake in a uniform density stratification is a convenient model problem to investigate the fluid dynamics of practical geophysical and nautical applications, such as the wakes generated by islands or the flow around submerged bodies. In addition to the Reynolds number, $Re = \rho UL/\mu$, a second dimensionless group characterises the relative strength of stratification, known as the internal Froude number, $Fr = U/NL$, where $N^2 = -(g/\rho_0)\partial\rho/\partial z$. Here, U and L are characteristic velocity and length scales in the flow, ρ_0 is a reference density, $\partial\rho/\partial z$ is the density gradient, g is the

† Email address for correspondence: geoff@usc.edu

acceleration due to gravity in the direction of the density gradient and μ is the dynamic viscosity of the fluid. For the particular case of the sphere wake, U and L are taken as the body speed and diameter, respectively. The internal Froude number is $Fr = 2U/ND$, based on radius, $D/2$, so the value $Fr = 1$ denotes the maximum resonance between a convective time and a buoyancy time, as explained in § 2.3.

After some time, initially turbulent wakes evolving in a background density gradient develop a regular pattern of alternating vortices whose origin can be traced back to instabilities in the developing shear layers (Spedding 2002). The coherent structures emerge during what has been termed the non-equilibrium regime (NEQ) as the density gradient increasingly exerts an influence on the fluctuating and then mean vertical velocities. This period of adjustment of the wake to its background begins at approximately $Nt = 2$, and ends at approximately $Nt = 50$, depending on the initial conditions. During this time, suppression of the fluctuating vertical velocity components reduces the associated Reynolds stress components and so decreases the kinetic energy dissipation rate (Brucker & Sarkar 2010; Redford, Lund & Coleman 2015). The vertical velocity fluctuations are diminished partly by the work required to lift fluid parcels from their equilibrium position, and partly because they can be removed from the wake as wake-generated internal waves. The energy contained in these waves, and removed from the wake, is an increasing fraction of the total as *Re* increases (Abdilghanie & Diamessis 2013; Rowe, Diamessis & Zhou 2020) and high-resolution simulations in Watanabe *et al.* (2016) demonstrated that the energy loss from wave radiation can be equal to the energy dissipated in turbulence in the wake itself.

1.2. *The influence of initial conditions*

After NEQ, the vortex motions persist. Streamwise averages of the mean and fluctuating velocities then yield statistically similar profiles in both lateral and vertical directions, and can be re-scaled based only on an effective drag coefficient (Meunier & Spedding 2004, 2006). In that case, the only amplitude variations come from the net horizontal momentum flux, and in all other respects the particular shapes have no far-wake influence. Instead, the dynamics is self-similar, much as the original hypothesis proposed by Townsend (1976) for three-dimensional turbulent wakes. However, even in unstratified turbulent wakes, the hypothesis has been called into question in experiment (Bevilaqua & Lykoudis 1978; George 1989) and in computations (Redford, Castro & Coleman 2012), which showed that differences in the wake structure far downstream could be traced back to differences in the initial conditions, affecting the evolution of mean and fluctuating quantities in differing ways.

Experiment and simulations agree on some approximate measures of the evolution of various length and velocity scales (Gourlay *et al.* 2001; Dommermuth *et al.* 2002; Brucker & Sarkar 2010; Diamessis, Spedding & Domaradzki 2011), but it is not easy to find general rules and predictions for when and how special features from initial conditions will prevent agreement. Early numerical simulations (Métais & Herring 1989) indicated that stably stratified turbulence-in-a-box would retain memory of different initial conditions (such as balances of vortical vs internal wave motions). On the other hand, the widespread emergence of late-wake coherent structures and similar wake growth/decay rates in simulations having widely differing initialisations (Gourlay *et al.* 2001; Dommermuth *et al.* 2002; Diamessis *et al.* 2011; Redford *et al.* 2015) suggests that the particular route to the late wake may well be unimportant.

1.3. *Scaling and turbulence in stratified wakes*

A scale similarity in strongly stratified wakes has been demonstrated analytically by Billant & Chomaz (2001) who showed that, when $Fr_h << 1$, a vertical length scale would be $l_v = U/N$, when energy is approximately equally partitioned between kinetic and potential energy. In that case a local Froude number based on vertical length scales and local fluctuating horizontal velocity, u_h, $Fr_v = u_h/Nl_v = O(1)$. Lindborg (2006) showed that the $Fr_v = 1$ invariance can alternatively be demonstrated as a consequence following the stipulation of energy equipartition. The dynamics of stratified turbulence is ultimately determined by the relative magnitudes of turbulent, buoyancy and viscous dynamics. Spedding (1997) proposed that turbulent stratified wakes evolve through three distinct regimes: a presumed three-dimensional (3-D) regime is initially unaffected by stratification, followed by a NEQ interval when buoyancy begins to significantly modify the dynamics then transitions into a flow state (Q2D) consisting mostly of 2-D motion, where the vertical velocity component, w, is small compared with $\{u, v\}$. The wake regime sequence of 3-D–NEQ–Q2D is based on wake-scale and mean quantities, which themselves are outcomes from local turbulence dynamics, as well as the initial forcing at U and D. If we define local Reynolds and Froude numbers based on horizontal integral length scales, l_h, so $Re_h = u_h l_h/\nu$ and $Fr_h = u_h/Nl_h$, then a combination of these yields a buoyancy Reynolds number,

$$\mathcal{R} = Re_h Fr_h^2, \qquad (1.1)$$

the magnitude of which measures the range of scales over which horizontal turbulent motions can occur, even while being constrained by the condition of strong stratification, when $l_v << l_h$ and $Fr_v = 1$. Lindborg (2006) showed that this kind of strongly stratified turbulence produces a forward energy cascade with horizontal wavenumber scaling of $k_h^{-5/3}$, as indeed measured in the atmosphere (Nastrom, Gage & Jasperson 1984; Nastrom & Gage 1985). Brethouwer *et al.* (2007) extended the analysis to show that flows for $\mathcal{R} >> 1$ are little affected by viscosity, and furthermore that within that regime there are two distinct sub-regimes. If we define an Ozmidov scale, $l_O = (\epsilon/N^3)^{1/2}$ as a scale where overturning motions are damped by stratification, and a Kolmogorov scale, $l_K = (\nu^3/\epsilon)^{1/4}$, as a small scale where viscosity consumes turbulent fluctuations, then there is a range $l_K \leq l_t \leq l_O$ where turbulence can proceed mostly unaffected by either stratification or viscosity, and another range $l_t > l_O$ where energetic turbulence is nevertheless strongly influenced by buoyancy. In many laboratory experiments, especially at late times, size limitations lead to $\mathcal{R} << 1$ and Godoy-Diana, Chomaz & Billant (2004) proposed that the observed independence of the late-time dynamics from Fr can be understood as a limit when flows reach a viscous-dominated attractor, although relevant scaling laws for a $\mathcal{R} >> 1$ state to reach the viscous regime could depend on the initial state.

Turbulence can occur in scales from l_K up to l_O, and de Bruyn Kops & Riley (2019) have drawn attention to a parameter we shall term $\mathcal{G}$, following early work by Gibson (1980) and Gargett, Osborn & Nasmyth (1984). Writing $l_O/l_K = \epsilon/N^2\nu$, then since a root-mean-scale (r.m.s.) turbulent length scale can be written as $l_t = u_t^3/\epsilon$, the scale ratio is

$$\mathcal{G} = \frac{\epsilon}{N^2\nu} = Re_t Fr_t^2, \qquad (1.2)$$

where Re_t and Fr_t are based on the r.m.s. turbulent velocity, u_t and l_t; $\mathcal{G}$ was described as an activity parameter in de Bruyn Kops & Riley (2019) and together with a local Froude number, its value can be used to separate dynamically dissimilar regimes as an initial turbulence decays against a stratified background. The expressions in (1.1), (1.2) depend

on l_h, u_h and l_t, u_t, respectively, where u_h is an r.m.s. velocity scale in the horizontal and u_t is the total r.m.s. velocity. The ratio of $\mathcal{G}/\mathcal{R}$ varies with time, and with Re (de Bruyn Kops & Riley 2019). The relationships between a dissipation rate, ϵ and other length and velocity scales is readily supported in strong, box-filling turbulence, but less clear in weaker turbulence that evolves in highly anisotropic fashion from its start. Wakes are also non-uniform in space, and measures such as $\mathcal{G}$ and $\mathcal{R}$ will be non-uniformly distributed across the wake, declining to zero outside it. Zhou & Diamessis (2019) considered these matters in some detail in temporal simulations that ran up to $Re = 4 \times 10^5$.

There is interest in how a turbulent stratified wake makes the transition from strongly stratified turbulence (SST) to viscous dominated and at what critical values of $\mathcal{R}_c$ and $\mathcal{G}_c$ the transition may occur. Rigorous estimates of $\mathcal{R}$ and $\mathcal{G}$ require accurate information at scales approaching l_K (Riley & de Bruyn Kops 2003; de Bruyn Kops & Riley 2019), and these authors explored how such criteria for different dynamical regimes could apply to experiments and simulations where only larger-scale information is known.

In a similar spirit, Zhou & Diamessis (2019) considered the regime $\mathcal{R} > 1$ and $Fr_h <<$ 1, (where the requirement on $\mathcal{R}$ is less stringent than the original $\mathcal{R} >> 1$ prescription) and interrogated simulations where $Re = [5k, 100k, 400k]$ and $Fr = [4, 16, 64]$. Intervals of Nt from 50 to 200 were identified where $Fr_v \approx 1$, but the measure declined steadily in all cases. If the conditions $\mathcal{R} > 1$ and $Fr_h << 1$ are used to define SST, then a threshold value based on initial parameters of $ReFr^{-2/3} \geq 5 \times 10^3$ was proposed. Body-inclusive simulations are reaching higher Re, with regions in the wakes that can claim to be fully turbulent and that then transition to SST states. Chongsiripinyo & Sarkar (2020) ran large eddy simulations to simulate a disk wake at $Re = 5 \times 10^4$, and described successive transitions from weakly stratified, to intermediate-stratified, to strongly stratified (WST–IST–SST) turbulence. This succession of regimes could be identified in localised regions of the disk wake and could be reached because the initial Re was comparatively high.

1.4. *Sphere wake regimes at low Re–Fr*

Early experiments on the wake of a sphere show a range of distinct shedding and wave regimes at comparatively low Re and Fr (Lin, Boyer & Fernando 1992; Chomaz *et al.* 1993). It is clear specific flow regimes can be established, although it is perhaps less clear how these specific flow regimes evolve far downstream. In particular, the claims of geometry independence (Spedding 1997; Meunier & Spedding 2004) can only be made for flows where initial $Re \geq 5000$ and $Fr \geq 4$ are high enough so that some scale independent turbulent motions can exist. Therefore, wakes with lower initial Re and Fr may then contain some details specific to the initial conditions downstream of the body. Xiang *et al.* (2015) have already shown that there are no universal characteristics in the near wake of a towed grid over a range $2700 \leq Re \leq 11\,000$ and $0.6 \leq Fr \leq 9$. Such a conclusion might be anticipated when the Re, Fr values extend so low. Numerical simulations that include the body (Orr *et al.* (2015), Pal *et al.* (2016), Pal *et al.* (2017), Chongsiripinyo, Pal & Sarkar (2017), Chongsiripinyo & Sarkar (2020) and Ortiz-Tarin, Chongsiripinyo & Sarkar (2019), the latter two are for a circular disk and a prolate spheroid, respectively) now reach $Re = 5 \times 10^4$, and much focus is on extending techniques to increase Re further. Here, we refocus on the sphere wake at moderate Re and Fr, using computational and experimental methods that match in parameter space to measure wake characteristics near the sphere and then extending to downstream distances where stratification begins to dominate.

1.5. *Objectives*

The purpose of this study is to systematically cover a region of $\{Re–Fr\}$ parameter space that covers a number of distinct regimes depending on the relative dominance of Fr or Re-dependent effects. The space $Re \in [200, 1000]$, $Fr \in [0.5, 8]$ contains completely laminar flows and those with irregular motion that are the first signs of turbulence. The parameter space also has flows that are strongly constrained by body-generated lee waves to those where the near wake is fully separated. There is explicit overlap with the flow visualisation experiments of Lin *et al.* (1992) (LI92) and Chomaz *et al.* (1993) (CH93), and with the numerical simulations of Orr *et al.* (2015) (OR15). Here, the focus is on independent and systematic variation of both Re and Fr in this parameter range, and numerical simulations and laboratory experiments were run together, under the same nominal conditions. The goal is to compare descriptions of the varying flow regimes within this study and with existing literature, and moreover to give quantitative descriptions of characteristic features. Ultimately we seek to predict when and if the quantitative data can be used to extract wake generator information from the wake signatures themselves.

2. Methods

2.1. *Numerical method*

Numerical experiments of the stratified sphere wake were solved using a finite volume solver in OpenFOAM. Given an initial stratification in the vertical (z) direction, the density and pressure, p, fields are decomposed into mean and fluctuating components given by (2.1) and (2.2), where x is the 3-D coordinate in space and t is time

$$\rho(\boldsymbol{x}, t) = \bar{\rho}(z) + \rho'(\boldsymbol{x}, t) \tag{2.1}$$

$$p(\boldsymbol{x}, t) = \bar{p}(z) + p'(\boldsymbol{x}, t). \tag{2.2}$$

Equations (2.3), (2.4) and (2.5) are the continuity, momentum and density evolution equations, solved under the Boussinesq approximation along with a hydrostatic balance term ($\partial \rho / \partial z = -g\bar{p}$) where $\boldsymbol{u}$ is the velocity, $\boldsymbol{g}$ is the gravitational acceleration in the direction of the density gradient, α is the thermal diffusivity and ν is the kinematic viscosity

$$\nabla \cdot \boldsymbol{u} = 0; \tag{2.3}$$

$$\frac{\partial \boldsymbol{u}}{\partial t} + \boldsymbol{u} \cdot \nabla \boldsymbol{u} = -\nabla p' + \nu \cdot \nabla^2 \boldsymbol{u} + \rho' \boldsymbol{g} \tag{2.4}$$

$$\frac{\partial \rho'}{\partial t} + \boldsymbol{u} \cdot \nabla \rho' = w \cdot \frac{\mathrm{d}\bar{\rho}}{\mathrm{d}z} + \alpha \cdot \nabla^2 \rho'. \tag{2.5}$$

Simulations were conducted at $Re = [200, 300, 500, 1000]$ and $Fr = [0.5, 1, 2, 4, 8]$. Both U and R are maintained at a constant value of 1 for each simulation, so changes to Fr are made by altering $\mathrm{d}\rho/\mathrm{d}z$ and changes to Re are made by altering ν. In a thermally stratified water column, the ratio of momentum to thermal diffusivity, as measured by the Prandtl number is $Pr = \nu/\alpha = 7$. In a salt stratification with molecular diffusivity, D_s, the equivalent Schmidt number is $Sc = \nu/D_s = 700$. The small-scale resolution requirements in the simulations thus rise accordingly, and here we set $Pr = 1$. The computations will not be expected to resolve the small scales of scalar gradients. Temporal and spatial derivatives are second-order accurate. Figure 1 shows the computational domain and observation window. The computational domain was $16D \times 16D \times 70D$ in the (y, z, x)
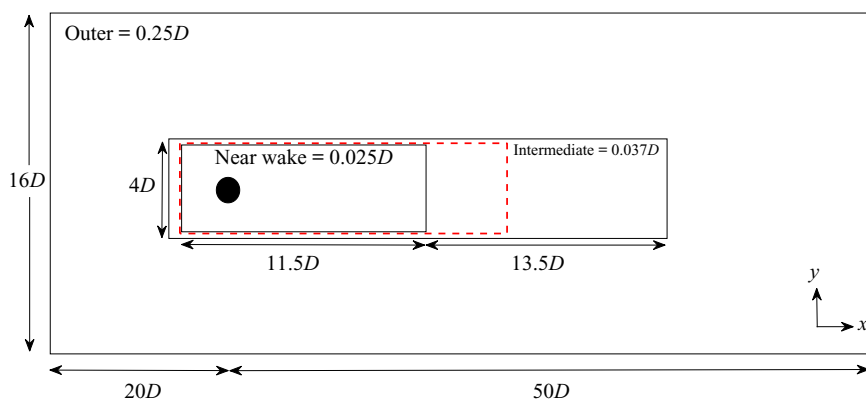
Figure 1. Computational domain for near-wake sphere simulations. Results are taken from a smaller domain outlined in red with dimensions $4D \times 4D \times 15D$, in the (y, z, x) directions respectively.

directions respectively. To focus on the near-wake properties, and to avoid possible boundary effects, measurements are only taken up to $x/D = 15$. A coarse mesh with 3 M cells was used for $Re = (200, 300, 500)$. A finer mesh with approximately 17 M cells is used for $Re = 1000$. The mesh is always finer close to the body: the near wake has 1.7 M cells in the coarse mesh and 11.8 M for the fine mesh. In order to reduce reflections from internal waves at the domain boundaries, zero gradient boundary conditions are adopted. The sphere is oscillated back and forth in each direction once to break flow symmetry (Lee 2000).

2.2. *Experimental set-up*

Experiments were conducted in a $1\,\text{m} \times 1\,\text{m} \times 2.5\,\text{m}$ tow tank. Stratification and optical access were achieved using a refractive index matched two-tank filling method (Xiang *et al.* 2015). The sphere was towed from right to left and was suspended from a translation stage with three thin wires of diameter, $d = 0.5\,\text{mm}$ as shown in figure 2; Re and Fr were kept near nominal values of $Re = [200, 300, 500, 1000]$ and $Fr = [0.5, 1, 2, 4, 8]$, matching the simulations. Each experimental run was performed a minimum of six times.

Table 1 shows the experimental parameters for each Re and Fr tested. The kinematic viscosity, $\nu = 1.0005 \times 10^{-6}\,\text{m}^2\,\text{s}^{-1}$. The temperature of the water was maintained near $25 \pm 1\,^\circ\text{C}$. Refractive index matching can cause variations in the kinematic viscosity. For $N = 0.37\,\text{rad s}^{-1}$ the salinity of the water at the bottom of the tank was $35\,\text{g NaCl kg}^{-1}$ H_2O. A transition from fresh water to a salinity of $35\,\text{g kg}^{-1}$ at $25\,^\circ\text{C}$ corresponds to a $\Delta\nu/\nu \approx 0.1$ over the height of the fluid (Nayar *et al.* 2016) for a possible 10 % variation in ν. The variations of ν over the diameter of the largest sphere are less than 2 %. Although flow transitions for sphere wakes, both stratified and unstratified, are sensitive to Re for $Re \leq 1000$, the difference in ΔRe from $\Delta\nu$ did not move the data from one flow regime to another in these tests.

The tank was filled with water/salt/alcohol to a height, $H = 80\,\text{cm}$, which ensured the centre of the largest diameter sphere was $3.6D$ away from both the free surface and the bottom of the tank. In this configuration the sphere travelled $10D$ before data acquisition. Data acquisition began when the centre of the sphere was in the middle of the field of view, which was set to a streamwise location to postpone contamination from start and end conditions. The startup transients in the wake propagate upstream, dragged there by the wake itself. When the sphere stops, the wake collides with the sphere, and any bow-wave
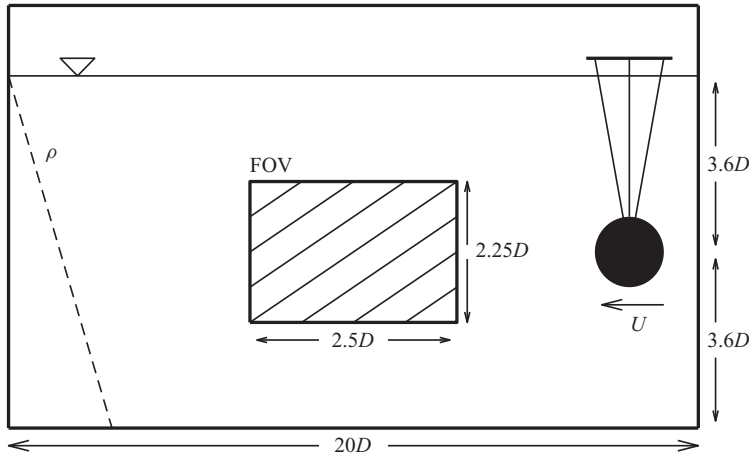
933 A12-6

Figure 2. Experimental set-up for sphere wake experiments. Distances shown are with respect to the largest diameter sphere tested, $D = 11.1$ cm.

	R2			R3			R5			R10		
	U	D	N	U	D	N	U	D	N	U	D	N
$F.5$	0.37	5.5	0.29	0.40	7.8	0.21	0.70	7.8	0.37	0.95	11.1	0.34
$F1$	0.53	3.9	0.29	0.55	5.5	0.21	0.99	5.5	0.37	1.41	7.8	0.37
$F2$	0.74	2.8	0.29	0.80	3.9	0.21	1.41	3.9	0.37	1.97	5.5	0.37
$F4$	1.03	2.0	0.29	1.16	2.8	0.21	1.91	2.8	0.37	2.81	3.9	0.37
$F8$	1.41	1.4	0.29	1.61	2.0	0.21	2.68	2.0	0.34	3.95	2.8	0.37

Table 1. Tow speed, U (cm s^{-1}), sphere diameter, D (cm), and buoyancy frequency, N (rad s^{-1}), for each experimental configuration. The naming convention $RxFy$ will be used for $Re = $ x00, $Fr = y$.

type conditions bounce off the front wall, and back into the sphere and wake. These effects limit the observation time window available. That time window depends on operating conditions, and is determined from flow visualisation experiments and then checked when practicable by ensuring statistical similarity at different x positions within the field of view (FOV).

Two components of velocity were obtained in the horizontal (xy) and vertical (xz) centreplanes using a planar particle imaging velocimetry system. The tank was filled with titanium dioxide particles with an average density of 4.23 g cm^{-3} and diameter of 15 μm. The image plane was illuminated with an Nd:YAG laser operated at a wavelength of 532 nm and a repetition rate of 20 Hz. Images were processed using a multipass algorithm with initial interrogation box size of 64×64 pix with 50 % overlap to a final box size of 32×32 pix. The box resolution therefore ranged from $0.05D$ to $0.22D$ in the horizontal plane.

2.3. *Analysis*

The averaged results from experiments are ensemble averages over all repeated experimental runs. Wake quantities are averaged with respect to the moving body for each

downstream position, x. In a vertical slice, the mean wake quantity can be written

$$\bar{q}(x) = \frac{1}{K} \sum_{i=1}^{K} q_i(x, 0, z),\qquad(2.6)$$

where $\bar{q}$ is the ensemble-averaged wake quantity at downstream location x, q_i is the instantaneous value at $x = (x, 0, z)$. Subscript i designates the laboratory reference frame of the data. For example $q_1(c, 0)$ is the first instance when wake data were available at downstream location $(c, 0)$. The parameter K is the total number of ensembles for a single run; $K = 100$ for the smallest diameter sphere and 54 for the largest. The ensemble averages for each experimental run are then averaged together over all runs. Figure 3 shows an example of three ensembles at downstream location $x = 0$ and $x = c$ for three laboratory reference frames. The same averaging technique is used in the horizontal plane,

$$\bar{q}(x) = \frac{1}{M} \sum_{i=1}^{M} q_i(x, y, 0),\qquad(2.7)$$

where, $\bar{q}(x)$, is the wake-averaged quantity at coordinates $x = (x, y, 0)$, and M is the total number of ensembles available in the horizontal plane for position x. In the horizontal plane M varied between 124 and 287 for the largest and smallest sphere cases, respectively. The r.m.s. fluctuating quantities based on temporal averaging in the vertical and horizontal plane are

$$q'(x) = \left[\frac{1}{K} \sum_{i=1}^{K} (q_i(x = (x, 0, z)) - \overline{q_i}(x))^2 \right]^{1/2}\qquad(2.8)$$

$$q'(x) = \left[\frac{1}{M} \sum_{i=1}^{M} (q_i(x = (x, y, 0)) - \overline{q_i}(x))^2 \right]^{1/2}.\qquad(2.9)$$

Vertical and horizontal half-wake heights and widths, L_v and L_h respectively, are calculated based on distance from the centreline to the point where the local time-averaged velocity is 15 % of the centreline velocity, $\bar{u} = 0.15 U_0$ (matching the criteria in Orr *et al.* 2015) with which we make comparison.

The buoyancy frequency, N, has units of rad s^{-1}, so a buoyancy time scale in seconds is $t_b = 2\pi/N$. The time required for a neutrally buoyant particle at mid-equator to move on a semi-circle around a sphere of diameter D is $t_c = \pi D/2U$. A maximum resonance between buoyancy-induced internal waves and displacement of fluid over the body occurs when the buoyancy time scale, t_b, is twice the convective time scale, t_c. Their ratio is then

$$\frac{t_b}{2t_c} = \frac{2\pi}{N} \frac{U}{\pi D} = \frac{2U}{ND},\qquad(2.10)$$

and a Froude number based on $D/2$ will equal 1 when $t_b = 2t_c$.

3. Results

3.1. *Wake structure*

The wake vorticity field will be described from the simulation results, since simulation and experimental results will later be shown to be similar. Figures 4 and 5 show
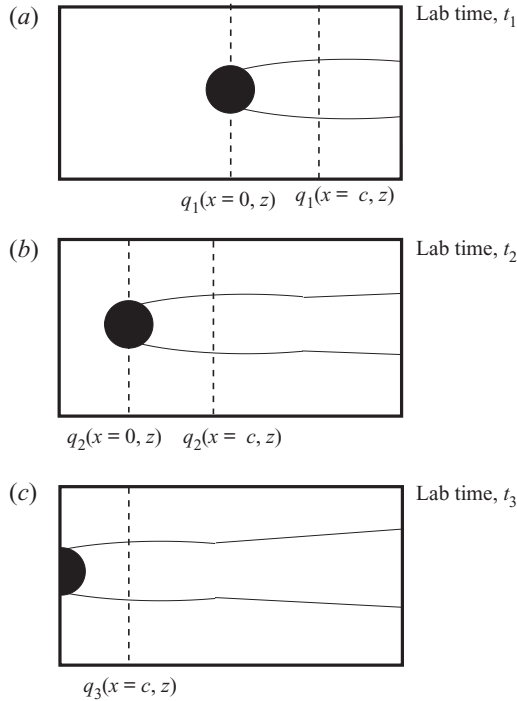
Figure 3. Example of wake quantity, q, ensembles at downstream locations $x = 0$ and $x = c$ as the sphere moves through the field of view in a fixed laboratory frame of reference; q could be a directly estimated quantity, such as $\{u, v, w\}$, or a derived measure from spatial derivatives.

the instantaneous vertical, ω_z, and lateral, ω_y, vorticity in the horizontal and vertical centreplane, respectively, at $Re = [200, 500, 1000]$ and $Fr = [0.5, 1, 8]$. All snapshots were taken at the same simulation time step $t^* = Ut/D = 75$.

In figure 4 there are distinct, and different, variations in the wake geometry for variations in both Re and Fr. The middle column, for $Fr = 1$, varies the least with Re. At this maximum resonance condition ((2.10), $t_b = 2t_c$) the lee waves control the conditions on the sphere and the wake is symmetric, at all Re, in both horizontal and vertical centreplanes (figure 5, centre column). As the stratification is relaxed ($Fr = 8$, right column), the centreline symmetry is maintained in both horizontal and vertical planes at low $Re = 200$, but is broken for $Re \geq 500$ (cases $R5$, $R10$ in the rightmost $F8$ column). In $F8R10$ there are strong gradients in both ω_z and ω_y, and evidence of a number of smaller scales of motion behind the sphere and in the developing wake.

When $Fr = 1$, the flow in the vertical centreplane travels around the sphere edge, rejoining almost at the equatorial plane. The dominant wavelength in the streamwise direction does not vary with Re (middle column, figure 5). In the left column of figures 4 and 5, $t_b \approx t_c$ and the preferred internal wavelength is shorter than a half-circumference, so the flow departs from the sphere at an azimuth angle of approximately $2\pi/3$. In the horizontal centreplane, the shear layers extend further downstream as the flow is forced to travel around the sphere, rather than above and below it. At all Re, the wake now destabilises in the horizontal, with high amplitude ($\xi > R$) excursions. The wavelength decreases with increasing Re. Pal *et al.* (2016) and Chongsiripinyo *et al.* (2017) also found a rebirth of turbulent fluctuations with decreasing Fr below 0.5 (at fixed $Re = 3700$), and
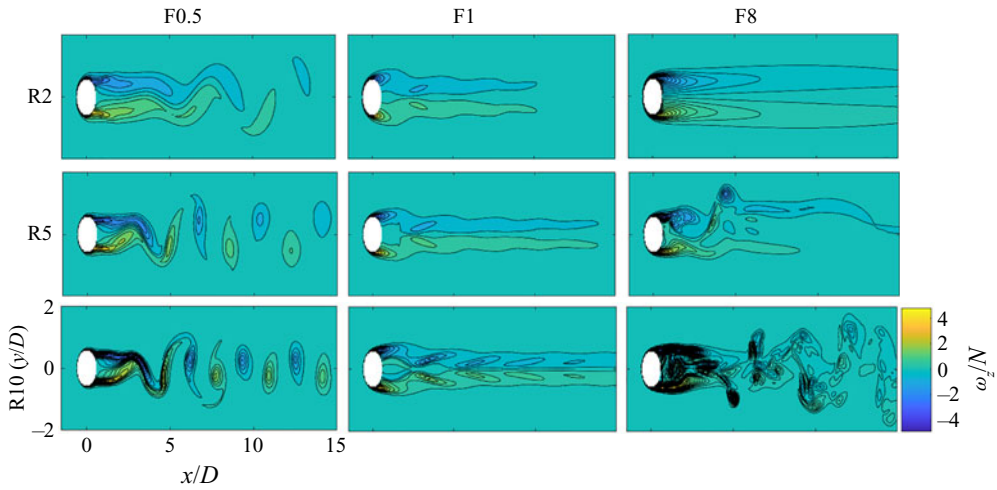
Figure 4. Vertical vorticity, $\omega_z(x, y)$ for $Re = [200, 500, 1000]$ and $Fr = [0.5, 1, 8]$ from simulations. Each plot has 10 evenly spaced contours over $\pm|\omega_z/N|_{max}$. The reference colour bar in the figure is for $F8R10$. Note that the vertical scale in y is expanded.
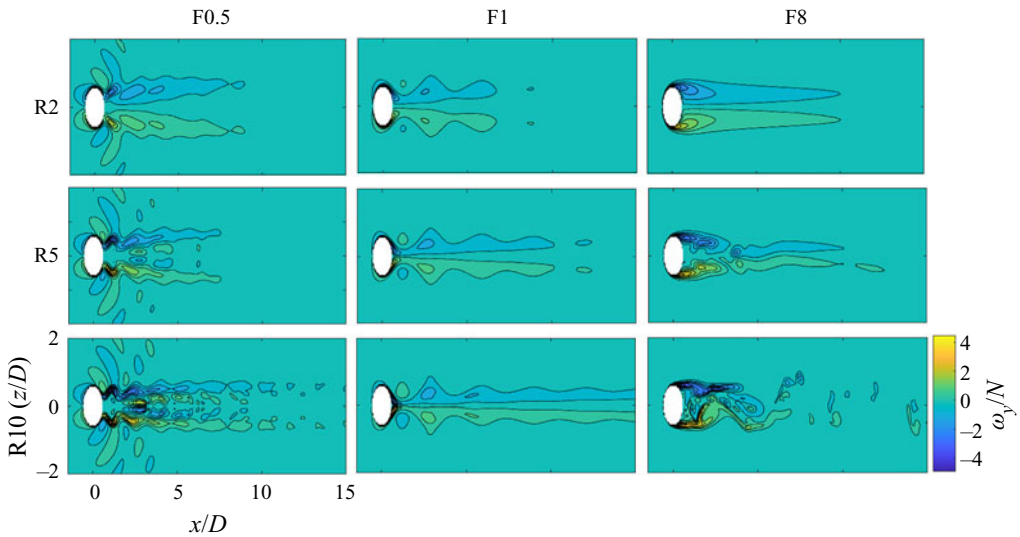

Figure 5. Lateral vorticity, $\omega_y(x, z)$ for $Re = [200, 500, 1000]$ and $Fr = [0.5, 1, 8]$ from simulations. Each plot has 10 evenly spaced contours over $\pm|\omega_y/N|_{max}$.

although Re here is insufficient to produce turbulence, the strong gradients in ω_z and in ω_y for $F.5R10$ (bottom left corner of figures 4 and 5) show the same, and somewhat counter-intuitive, consequence of the quasi-2-D forcing.

The qualitatively different wakes in figures 4 and 5 are placed in a $\{Re–Fr\}$ diagram and compared with the observations from CH93 in figure 6. A classification of the wakes from both experiment and simulation is shown by coloured symbols. For $Fr \leq 1$, variations in Re were not important and the wakes transition from steady, planar symmetric (red) to unsteady vortex shedding (purple) as Fr decreases from 1. The regimes from CH93 are saturated lee wave, and two-dimensional, the latter since the centreplane and nearby
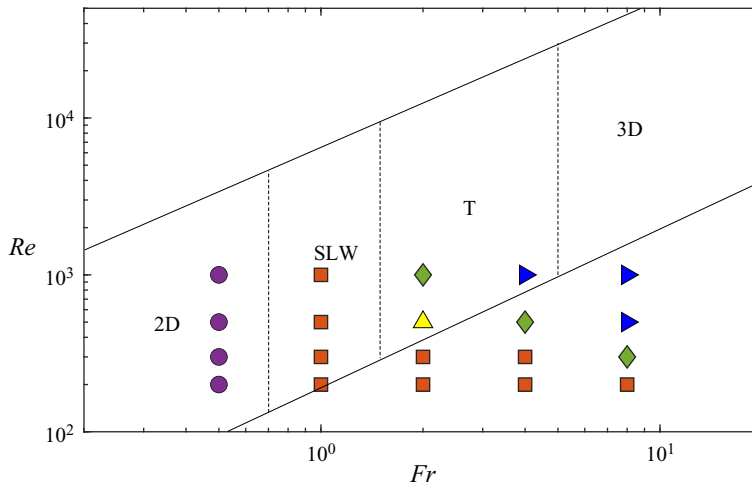
Figure 6. The {Re, Fr} regime diagram for the current experiments (coloured shapes) and from CH93 (background). CH93 divided the space mainly by Fr into four main subregions: two-dimensional, saturated lee wave (SLW), transition (T) and three-dimensional (3-D). The vertical dashed lines bound each subregion in Fr, Re space. The symbols denote wake structure across Fr, Re for the present study: horizontal vortex street (purple circles), steady, planar symmetric (red squares), vertical asymmetric (yellow triangle), planar oscillation (green diamonds) and multiple unsteady modes (blue right facing triangle).

layers generate vortex wakes much as a 2-D cylinder would. For $Fr = 2, 4$ the CH93 classification was of a transitional regime (T) without, and then with Kelvin–Helmholtz (KH) instability with increasing Fr. In the current study, there is a variation with Re at these intermediate Fr, and the wakes at $Fr = 2$ can be planar symmetric (red), vertically asymmetric but horizontally symmetric (yellow) or planar oscillating (green, the equivalent of KH in T). The planar oscillation is seen at higher Fr, lower Re also, in regions that lie outside the experiments of CH93. Multiple unsteady modes appear at higher Fr (blue), at lower Fr for higher Re. The detailed studies of LI92 and CH93 paid close attention to conditions on the sphere, especially at low {Re, Fr}. Here, we are mostly concerned with the pattern and geometry in the intermediate wake (omitting details of recirculation and separation zones) that then may, or may not persist into later times. In this respect, we note that the wake decay at large x could be enhanced in figures 4, 5 through numerical diffusion in the low-order method. The regimes identified are qualitatively consistent with existing literature, and the flow fields and their parametric variations can now be examined quantitatively

3.2. *Time-averaged wake properties*

3.2.1. *Streamwise velocity comparison*

Figure 7(*a,c,e,g*) shows the time-averaged streamwise velocity, $\bar{u}/U$, for simulations and experiments (*b,d,f,h*) in the vertical centreplane for constant $Fr = 1$ and varying Re. The most prominent feature at $Fr = 1$ is the lee wave which causes an initial decrease in wake height just behind the sphere. The amplitude of the contraction increases with increasing Re. The contraction occurs with a local minimum in the streamwise centreline velocity and has been observed at $Re > 1000$ for spheres (Bonnier & Eiff 2002; Pal *et al.* 2017) and behind towed grids (Xiang *et al.* 2015). The minimum $\bar{u}$ occurs at $x/D = 1.5$ for all Re simulations and at $x/D = 1.3 \pm 0.1$ for the experiments. The spacing and amplitude
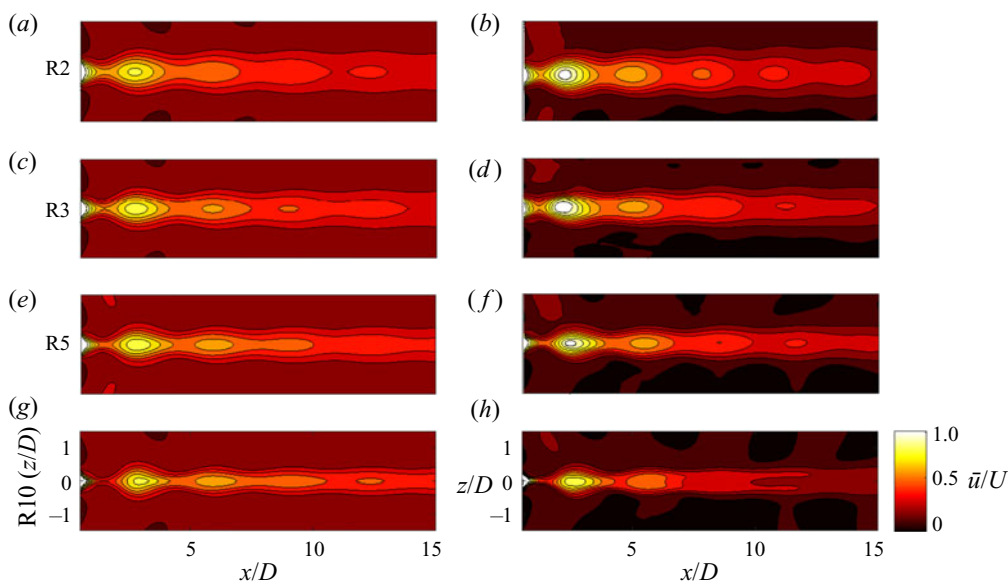
933 A12-11

Figure 7. Time-averaged streamwise velocity, $\bar{u}/U(x, z)$ for $Fr = 1$ and $Re = [200, 300, 500, 1000]$. Simulations are in ($a,c,e,g$), laboratory experiments are in (b,d,f,h). Each case has 10 evenly spaced contours between $\bar{u}_{max}$ and $\bar{u}_{min}$.

of the wake pulsations is unaffected by Re. The background level in experiments is lower (darker) because very small pixel displacements are on average drawn back to 0 due to peak locking.

Figure 8 shows a similar comparison at fixed $Re = 500$ and varying Fr. As Fr increases, so does the wavelength, λ, of the lee waves; x/D can be related to a buoyancy time, Nt through $x/D = NtFr/2$, and the minimum in $\bar{u}$ occurs at $Nt = 3.3 \pm 0.3$ and $Nt = 3.2 \pm 0.3$ for simulations and experiments, respectively at $Fr = [1, 2, 4]$. At $Fr = 8$, the minimum would be expected at $x/D = 25$, which is outside the observation windows in figure 8. The location of $\bar{u}_{min}$ agrees with towed grid experiments where $\bar{u}_{min}$ was found between $3 \leq Nt \leq 4$ for $2700 \leq Re \leq 11000$ and $0.6 \leq Fr \leq 9$. The wavelength λ is expected to be a linear function of Fr, $\lambda = \pi Fr$ as verified later.

3.2.2. *Mean velocity profiles*

Figure 9 shows the mean streamwise velocity profiles at several downstream locations rescaled by the local centreline value, $\bar{u}/U_0$, in both the vertical and horizontal centreplanes for $Re = 1000$, $Fr = 8$. The vertical and horizontal coordinates are normalised by the local half-height and width, L_v and L_h, respectively. In the vertical centreplane there is good agreement between the simulations and experiments, although for positive values of z/L_v the profiles from experiments do not fall to zero. The defect is caused by the wakes of the tow wires, which otherwise appear to be superimposed upon the mean wake with no other effect. The mean wake profile shapes are not otherwise distinguishably different from each other, over $x/D = [4–15]$.

Initially the horizontal plane velocity profiles in figure 9(b), are more varied, and the peak values of $\bar{u}/U_0$ may be off centreline, as also found in OR15 for $Re = 1000$, $Fr \geq 4$. The horizontal profiles reach a similar state by the end of the simulation domain. For this particular case $x/D = 8$ corresponds to $Nt = 2$, when buoyancy effects are thought to become significant, and vertical and horizontal profiles, although similar, are not the same.
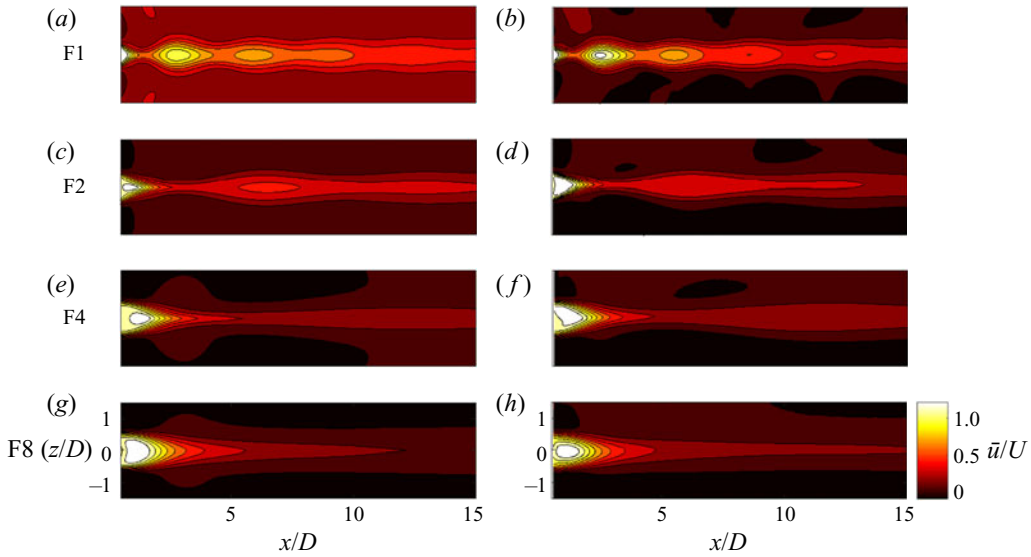
Figure 8. Time-averaged streamwise velocity, $\bar{u}/U(x, z)$ for $Re = 500$ and $Fr = [1, 2, 4, 8]$. Conventions are same as in figure 7.
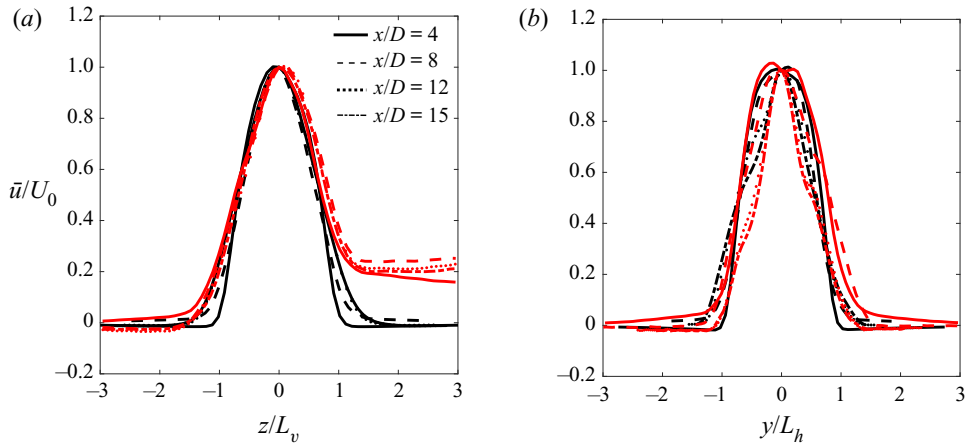

Figure 9. Rescaled streamwise velocity in the vertical (*a*) and horizontal (*b*) centreplanes for $Re = 1000$ and $Fr = 8$. Black and red lines correspond to simulations and experiments, respectively.

Figure 10 shows rescaled velocity profiles from experiment further downstream at $x/D = [15, 20, 25, 30]$ for the horizontal and vertical centreplanes. Profiles in the vertical plane retain their shape even at $x/D = 30$. At the furthest x/D observed the horizontal plane profiles have a similar shape to the velocity profiles in the vertical plane. The similar profile shapes encourage a search for regularities that govern the time evolution of length and velocity scales.

3.2.3. *Wake length scales*

Figure 11 shows the variation in vertical length scales with Re and Fr, and for experiment and simulation. The agreement between experiment and simulation is satisfactory, as the
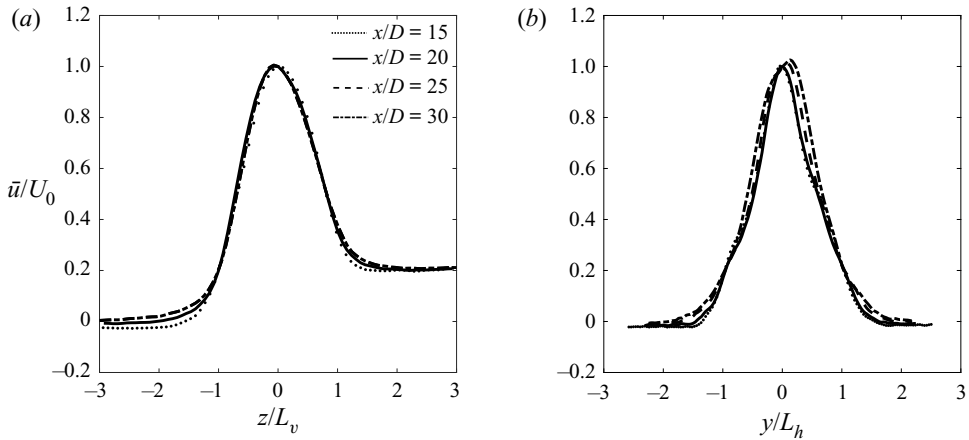
933 A12-13

Figure 10. Rescaled streamwise velocity profiles farther downstream in measurements from horizontal and vertical centreplane experiments for $Re = 1000$ and $Fr = 8$.
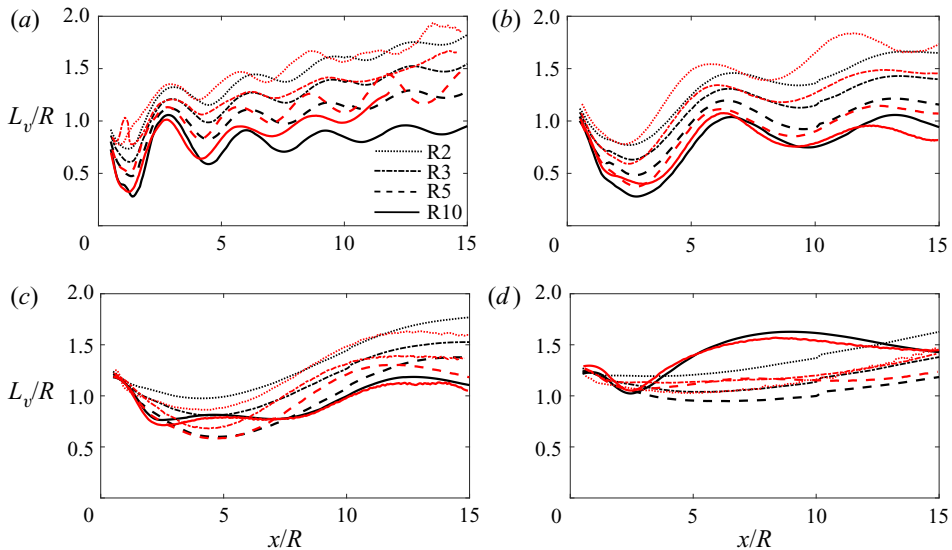

Figure 11. Downstream evolution of L_v/R for simulations (black lines) and experiments (red lines); (*a*) $F1$, (*b*) $F2$, (*c*) $F4$, (*d*) $F8$.

amplitudes and wavelengths together with variations in governing parameters are the same. At the lowest $Fr = 1$, local wake heights are strongly shaped by lee waves initiated at the body. For each $\{Re, Fr\}$ pair, the internal wave oscillation is superimposed on a gradual growth in L_v. At lower Re, L_v almost doubles over $x/D \approx 15$. Higher Re wakes have smaller L_v and they grow less rapidly in x, as seen qualitatively in figure 7. At higher Re, kinetic energy can be driven towards small-scale mixing, rather than slow laminar growth in an internal-wave-dominated near field. The vertical growth is strongly limited by the background stratification when everywhere $Fr \leq 1$.

As Fr increases, the wavelength and amplitude of the wake disturbances increase. At $Fr = 8$ the Re trend abruptly reverses as now higher Re leads to higher L_v. At $Re = 1000$, L_v increases at first, and then stays almost constant. This region of constant L_v was

933 A12-14

found by Spedding (2002) where the first available measurements were at $x/D = 10$. This almost constant $L_v(x/D)$, even decreasing slightly at first, can also be seen in Diamessis *et al.* (2011), where the initial height increases with *Re*, and in Dommermuth *et al.* (2002), Brucker & Sarkar (2010) and Zhou & Diamessis (2019). Reports of $L_v(x)$ vary considerably in detail in the literature (ops cit.), with variations from both *Fr* and *Re*. Differing physical mechanisms could be behind similar L_v observations, and Meunier, Diamessis & Spedding (2006), for example, contend that the low-growth region is only a consequence of the slow transition between turbulent and viscous scaling regimes.

It has been noted before (Spedding, Browand & Fincham 1996*b*) that a lower limit on *Fr* that allows turbulence over some range of scales can be estimated through the Ozmidov scale, l_0, the largest overturning scale allowed by the stratified ambient

$$l_0 \sim \left(\frac{\epsilon}{N^3}\right)^{1/2}, \tag{3.1}$$

where ϵ is the kinetic energy dissipation rate. In homogeneous turbulence $\epsilon \sim u'^3/l$, where u' is a fluctuating velocity and l an integral length scale so

$$l_0 \sim \left(\frac{u'^3}{lN^3}\right)^{1/2}. \tag{3.2}$$

For turbulent scales of l to be initially unaffected by the stratification, $l_0 \geq l$ and

$$\left(\frac{l_0}{l}\right) = \left(\frac{u'}{U}\right)^{3/2} \left(\frac{l}{D}\right)^{-(3/2)} \left(\frac{U}{ND}\right)^{3/2} \geq 1. \tag{3.3}$$

In unstratified sphere wakes (Gibson, Chen & Lin 1968; Uberoi & Freymuth 1970), $u'/U \approx 0.3$ and $l/D \approx 0.4$ so

$$\left(\frac{U}{ND}\right)^{3/2} \geq 5, \quad Fr \geq 3. \tag{3.4a,b}$$

These arguments are concerned with when a minimum range of length scales for turbulent energetics could be expected, hence when the turbulent dynamics may explain wake length scales. Here, the {*Re–Fr*} range covers a region mostly in laminar and stratification-dominated wakes, and the strong influence of the body-generated lee wave can be seen throughout figure 11. Figure 12 shows the first minimum half wake height $(L_v/D)_{min}$ as a function of *Fr* for all the simulations. When $Fr < 4$, $(L_v/D)_{min}$ decreases as *Re* increases. For $Fr \geq 4$ the vertical scales can be influenced by the first signs of turbulence, and the differences in $(L_v/D)_{min}$ with *Re* begin to shrink. Computations at higher $Re \in [1, 4 \times 10^5]$ (Zhou & Diamessis 2019) show that *Fr* is less influential in determining vertical scales as *Re* increases, perhaps because the evolving flow has spent longer at $\mathcal{R} > 1$.

The mean wake height (minus lee-wave-induced oscillations) increases with downstream distance, and given the similar forms of the velocity profiles found in figures 9 and 10 we may find a power law of the form $L_v/D \approx \alpha(x/D)^\beta$. Table 2 shows the fitting coefficients, α and β, for the simulations and experiments. The average growth rate, β, for the simulations is $0.29 \pm .05$ and for the experiments is $0.27 \pm .06$. These wake growth rates do not show a clear dependence on either *Fr* or *Re*. They have been measured at x/D much smaller than previous experimental vertical stratified wake data (Spedding 2002). Pal *et al.* (2017) have measured L_v in a sphere-inclusive simulation but did not attempt a parametrisation. Chongsiripinyo *et al.* (2017) have given detailed descriptions of the vortex
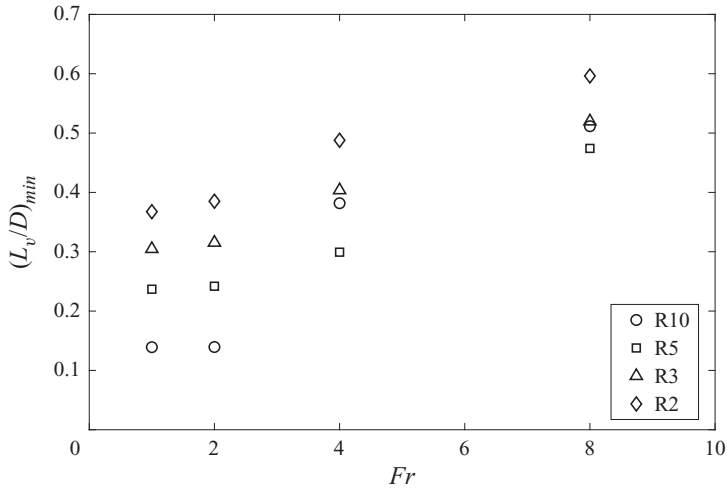
Figure 12. Vertical wake half-height, $(L_v/D)_{min}$ for simulations as a function of Fr. Re are given by the symbols in the legend.

	$Re = 200$				$Re = 300$				$Re = 500$				$Re = 1000$			
Fr	α	β	α_e	β_e	α	β	α_e	β_e	α	β	α_e	β_e	α	β	α_e	β_e
1	0.85	0.27	0.52	0.22	0.76	0.79	0.31	0.25	0.68	0.23	0.68	0.30	0.59	0.17	0.68	0.29
2	0.74	0.30	0.90	0.23	0.66	0.28	0.67	0.28	0.58	0.27	0.74	30	0.42	0.32	0.60	0.32
4	0.78	0.27	0.75	0.26	0.71	0.24	0.60	0.30	0.58	0.26	0.62	0.27	—	—	0.36	0.26
8	0.62	0.35	0.57	0.25	0.50	0.37	0.50	0.27	0.51	0.31	0.56	0.21	—	—	0.6	0.32

Table 2. Power law coefficients for wake height, L_v, for all Re and Fr found from simulation results; α_e and β_e are coefficients for the experiments.

dynamics and structures, focusing on $Fr < 1$, pointing out that the near-wake structures would be essential in carrying information from the near wake into the later stages of development.

It is clear that vertical length scales in the stratified wake can show significant variation with both Re and Fr, and that the relative importance of turbulent motions then also delineates regimes where $\mathcal{R}$ is large or small. Furthermore, it is also likely, given the different literature findings, that initial conditions play an as-yet unexamined role. We shall return to this topic in the discussion section.

The lee wavelength, λ, was determined from the streamwise distance between extrema in x of the half-wake height. Figure 13 shows the normalised lee wavelength as a function of Fr for the $R10$ simulations and experiments. In a linear density gradient, the natural cyclic buoyancy frequency is $N/2\pi$, and the wavelength is then $\lambda = 2\pi U/N$ or $\lambda/D = \pi Fr$, independent of Re. This relationship accounts well for the observations from experiment and simulation, and from measurements from Meunier *et al.* (2018) for $Fr \leq 2$. When $Fr > 2$, the experiments, simulations and Meunier *et al.* (2018) still agree but are slightly larger than the values predicted by linear theory.

Figure 14 shows the downstream evolution of the half-wake width, L_h/R. The $L_h(x)$ curves are qualitatively different, depending on Fr. At low $Fr \leq 4$ the same footprint of
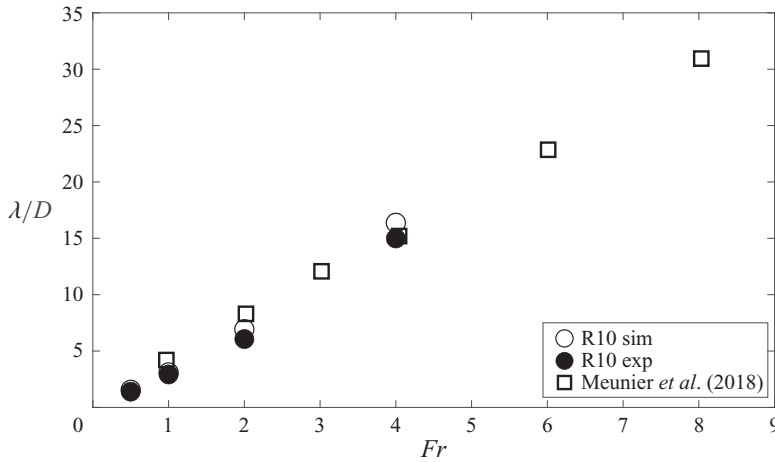
933 A12-16

Figure 13. Wake wavelength, λ/D vs Fr for $R10$ simulations, experiments and from Meunier *et al.* (2018).
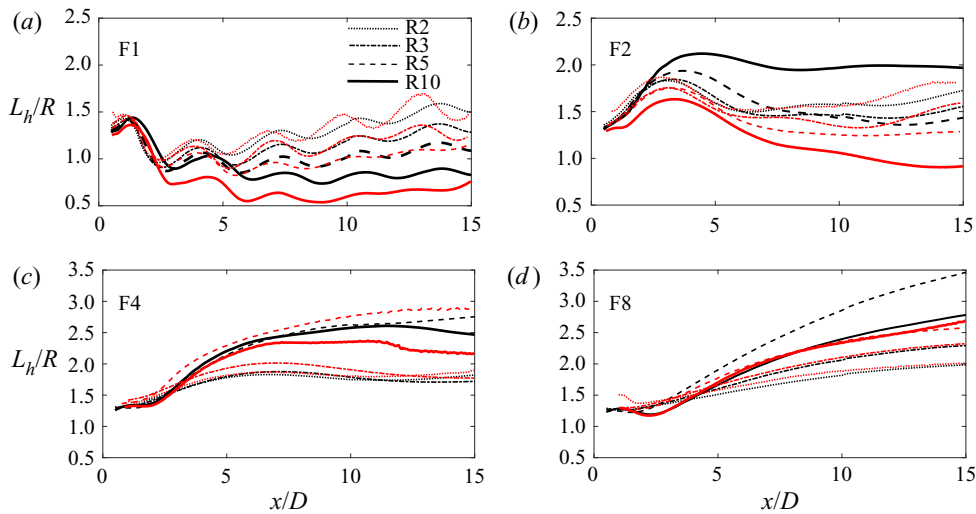

Figure 14. Wake width, L_h/R from experiment and simulation for $Fr = 1, 2, 4, 8$ in $(a–d)$. Simulations are in black, experiments in red.

lee waves as seen in figure 11 occurs in L_h (cf. figures 7 and 8). Only when $Fr = 8$ do the curves show a more gradual increase. There are significant differences between experiment and computations over the intermediate ranges $Fr = 2, 4$ and $Re = 500, 1000$. The $F2R10$ case has been re-run and investigated closely, and the differences remain. The L_h measure is affected by the unsteadiness in the simulation, which is not present in experiment, or in the simulations of OR15. The unsteady solution appears to be affected by the startup conditions where the sphere is accelerated back and forth, sending this borderline case to the KH regime rather than a regime without KH modes (SKH). The $F8R5$ curves differ because the grid resolution was too low as the emerging turbulence generates smaller scales. In general, the solutions for experiment and simulation match closely.

3.2.4. *Centreline velocity*

Figure 15 shows the mean centreline velocity evolution, (U_0/U) vs (x/D) for various Re and Fr combinations in simulation and experiment. At the lower Re (figure 15a) and lower
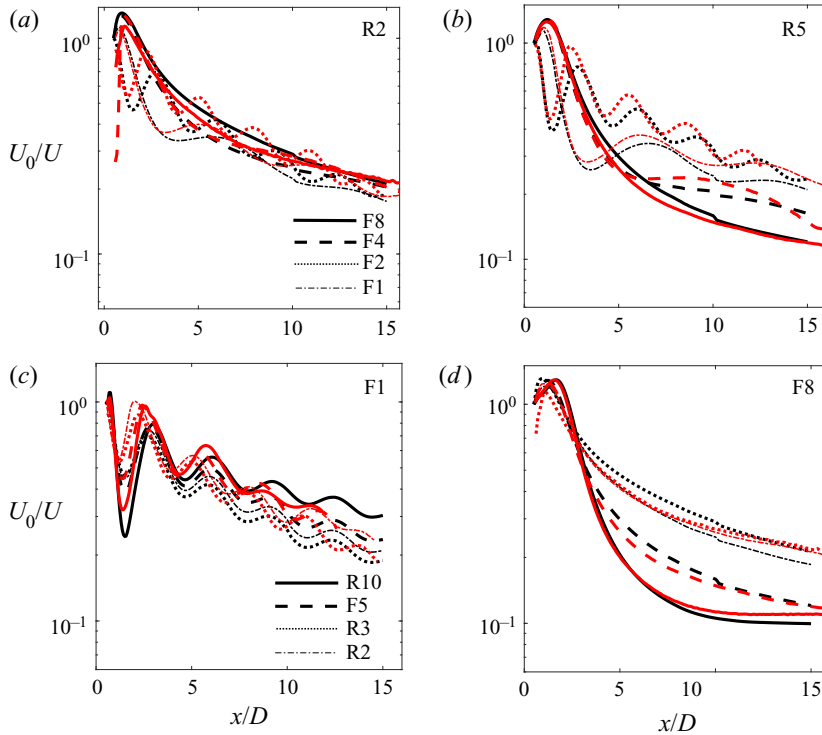
Figure 15. Downstream evolution of the normalised mean centreline velocity, U_0/U for (*a*) $Re = 200$, (*b*) $Re = 500$, (*c*) $Fr = 1$, (*d*) $Fr = 8$. Simulations in black, experiments in red.

Fr (figure 15*c*), there is no strong dependence on either *Fr* or *Re*. At $Fr = 1$ (figure 15*c*), the lee waves are the dominant influence, and U_0 cycles up and down out of phase with the product of $L_h L_v$, as required for continuity. These fluctuations at lower *Re*, *Fr* have been referred to as wake collapse (cf. Bonnier & Eiff 2002; Xiang *et al.* 2015) although nothing is collapsing (figures 11 and 14) and the oscillatory function lies on top of a gradual and uniform decay. At higher *Re* and higher *Fr* there is a single rise in U_0 and then a decay with x/D that is more pronounced at higher *Fr* and *Re*, respectively.

There is good agreement between experiment and simulation for $U_0(x)$, better than for the L_h measure, supporting the idea that the physics computed and measured are the same, but some averaging processes are less robust in limited averaging domains.

Early work on stratified sphere wakes had no means of reliably measuring wake characteristics at early times because the apparatus could not readily deploy refractive index matching, and the earliest measurement times were at $Nt \approx 10$. From these times onward, it was notable, and curious, that the mean and turbulence quantities then seemed to evolve according to power laws which could be written in terms as though the influence of stratification (through *Fr*) were negligible. Then, since $x = Ut$, we can make the equivalence $x/D = (Nt)Fr/2$ and expressions of the form

$$\left.\begin{array}{l} \dfrac{U_0}{U} = \alpha \left(\dfrac{x}{D}\right)^{\beta} \\[2ex] \dfrac{U_0}{U} Fr^{-\beta} = \alpha \, (Nt)^{\beta} \end{array}\right\}, \tag{3.5}$$
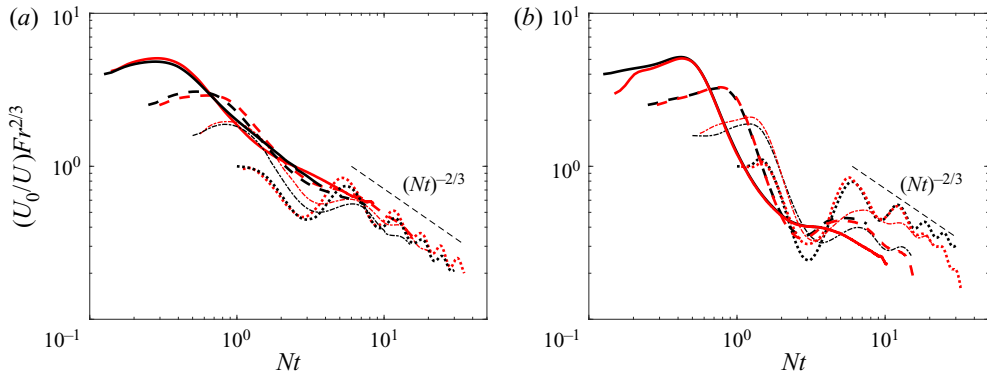
933 A12-18

Figure 16. Rescaled centreline velocity, $(U_0/U)Fr^{-2/3}$ for (*a*) $Re = 300$ and (*b*) $Re = 1000$ vs buoyancy time scale, Nt, for $Fr = 1, 2, 4, 8$. Solid, dash, dash-dot and dotted lines correspond to $Fr = 8, 4, 2, 1$, respectively.

can be written. The exponent β does not change between the two forms, and the only difference is the position in x/D or Nt for the data, which depends on Fr. In stratified flows that decay and eventually come under the leading influence of buoyancy, one might expect Fr-independent, 3-D dynamics first and then when buoyancy enters, it may do so at some fixed Nt. Instead, Fr-independent power laws were measured even at late times. The Fr-independence in strongly stratified turbulence was explained and predicted by Billant & Chomaz (2001), when $l_v = U/N$. Here, we are interested in when the initial early wake transitions into NEQ and Q2D states, so it is useful to plot a rescaled $U_0(Nt)$.

Figure 16 shows the evolution in Nt of the centreline velocity for $Re = 300, 1000$ with varying Fr. Here, the wake defect is just emerging into the Nt domain ($Nt \approx 3$) where previous experiments made their first measurements (Spedding 2001). The data do not show a low decay rate that has classically described the NEQ regime, but at low and high Re emerge at approximately $Nt = 10$ with a decay law that is similar to $-2/3$ (-0.66 ± 0.14 and -0.63 ± 0.11) for simulation and experiment, respectively. Spedding, Browand & Fincham (1996*a*) found NEQ–Q2D scaling only for $Re \geq 4000$, so the rather moderate success in collapsing U_0 at $Re = 1000$ is not in conflict. If the early signs of $-2/3$ decay are correct, then, if applicable, they must describe a regime that precedes the previously measured wakes. Although the decay rates are the same as for a turbulent, unstratified wake, the non-negligible influence of the stratification has been evident in all the preceding data.

3.3. *Fluctuating velocities and the buoyancy Reynolds number*

The maximum Re here, based on the sphere diameter and tow speed, is 1000, and the flow can hardly be considered turbulent. However, all decaying wakes, globally, or locally, will eventually enter a stage in which Re is small, so there is some interest in what fluctuating quantities look like even at small Re. Then the questions arise as to how this state was achieved and whether the origin from a higher energy state is relevant.

In this experiment, fluctuating quantities as defined in (2.8) and (2.9) can come from two sources: one is from unsteady activity in the wake at large scales, where coherent structures pass through measurement points, or volumes. The second is from fluctuations that derive from the turbulent dynamics. Referring to figures 4 and 5, only the lower right corner could qualitatively be described as turbulent, although it is easy to see how non-negligible fluctuations will occur in other situations, such as for $Fr = 0.5$. The measurements of
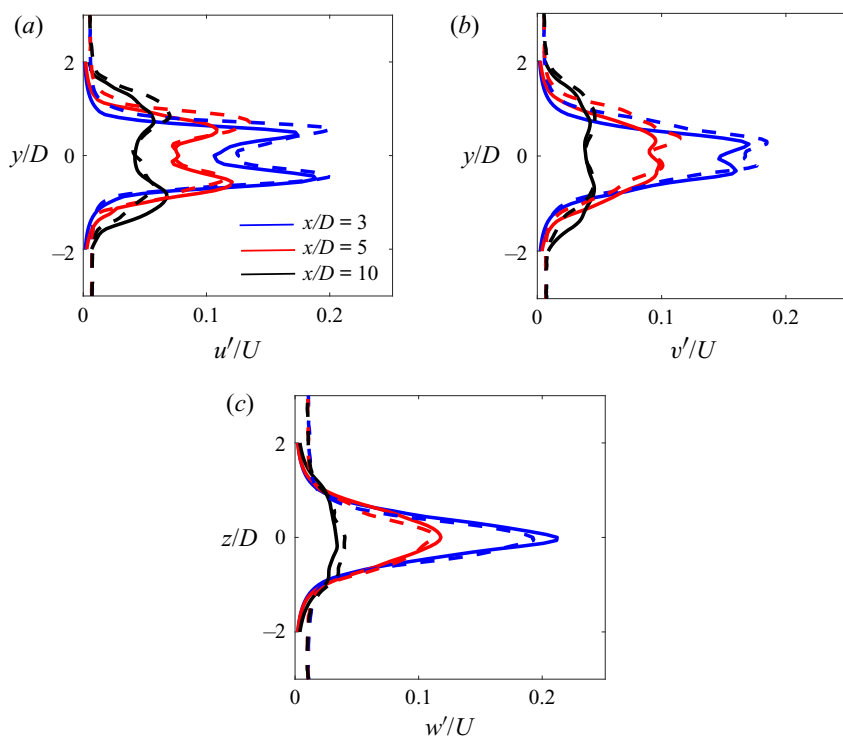
Figure 17. Fluctuating velocity components (a) $u'(y)$, (b) $v'(y)$ and (c) $w'(z)$ for $Re = 1000$, $Fr = 8$. Simulations and laboratory experiments are represented by solid and dashed lines, respectively.

u', v', w' described here are therefore not measures of turbulence, but are diagnostic measures of these early wakes in their various {Re–Fr} states.

Figure 17 compares {u', v', w'} at three downstream locations, $x/D = [3, 5, 10]$ for $Re = 1000$ and $Fr = 8$. At each downstream location the simulations and experiments agree well. The magnitude of the peaks of the streamwise fluctuations decreases with downstream distance while the width of the peaks increases as the wake width increases. $u'(y)$ has a double-peaked profile, as would be obtained when fluctuating quantities are associated with mean shear. $v'(y)$ has a similar shape although with smaller-amplitude peaks. $w'(z)$ has only a single maximum, which decays faster with x/D than the horizontal components. The first turbulence profiles for a stratified wake (Spedding 2001) were measured at $x/D = 6$ (or $Nt = 9$) and all three fluctuating velocity components were initially double peaked. The difference comes from Re, which was 5000 in the previous study, and 1000 here.

The dependence of the velocity fluctuation magnitudes on Re and Fr is shown in figure 18. At $Re = 300$ w'_0 falls almost immediately to approximately 1 % of u'_0, for all Fr. At $Re = 1000$ the $Fr = 4, 8$ cases remain at $w'_0/u'_0 \approx 1$ up to $x/D = 15$. There are fluctuations in the ratio with wavelength equal to the lee wavelengths. The averages are temporal averages so the lee waves themselves, which are steady in the sphere reference frame, do not directly contribute to w'_0, but some components of this wave-induced field clearly impact the measurement. In this respect then, all wakes are buoyancy influenced at all times.

It is useful to locate the sphere wakes discussed here in $Fr_h - \mathcal{G}$ space described by de Bruyn Kops & Riley (2019). The wake properties are not uniform so we make local
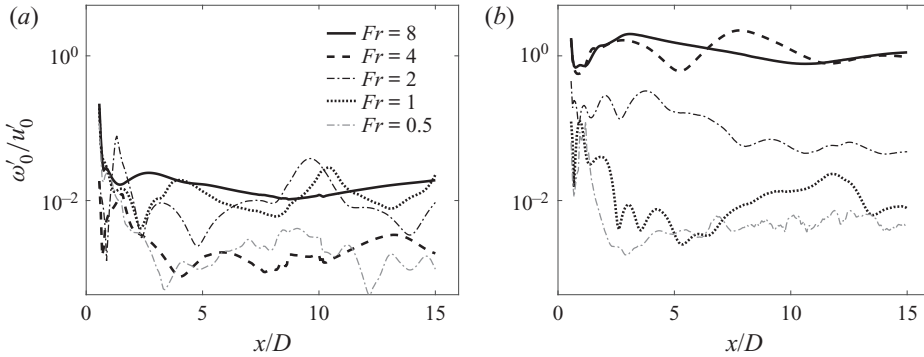
933 A12-20

Figure 18. Ratio of centreline fluctuations w'_0/u'_0 for (a) $Re = 300$ and (b) $Re = 1000$ for varying Fr, as given in legend of (a).

measures as explored and detailed in Xiang *et al.* (2015) and Zhou & Diamessis (2019). The latter authors proposed a criterion of $ReFr^{-2/3} \geq 5 \times 10^3$, based on initial wake parameters, D and U, could be used to indicate activity in a strongly stratified regime ((1.2) and after). At the highest $\{Re, Fr\}$ combination here $ReFr^{-2/3} = 250$, far below the suggested criterion. The relationship is counter-intuitive, however, as the product $ReFr^{-2/3}$ decreases for increasing Fr and fixed Re. Thus for $Fr = 1$, the product is 1000, while for $Fr = 32$, it is 100. This is because the quantity $\mathcal{G}$ aims to give relations when stratification is strongly felt, yet Re is still high, and blindly following this prescription would indicate that the $R10F1$ case is closer to SST than is $R10F8$. This cautionary note notwithstanding, we may make some local calculations, close to the wake edge, in order to estimate both $\mathcal{G}$ and Fr_h. The reasoning follows the arguments of Billant & Chomaz (2001) who show that there is a limit where a strongly stratified flow adjusts so that $Fr_v = 1$, when $l_v = U/N$. The length scale evolution is then indicated by $Fr_h = u'/Nl_h$, where l_h is the local horizontal length scale. This measure is derived from autocorrelations of time series of w'. The autocorrelation is plotted vs the lag number and the distance to the first zero crossing of the autocorrelation function is multiplied by the time interval, expressed as t_{loc}. Then the associated local horizontal length scale, $l_h = u't_{loc}$. The process is similar to that used by Diamessis, Gurka & Liberzon (2010) and Xiang *et al.* (2015), and is repeated for each experimental run and then averaged over all runs. If we retain the local u' as a measure of the available kinetic energy in velocity fluctuations, and we keep l_h as an indicator of turbulent length scales, then

$$\left.\begin{array}{l} Fr_t = \dfrac{u'}{Nl_h} \\[2mm] Re_t = \dfrac{u'l_h}{\nu}, \end{array}\right\} \tag{3.6}$$

and $\mathcal{G}$ can be calculated from (1.2) without direct recourse to assumptions about the isotropy of ϵ, for example. We may note that variations in ρ and its gradient $\partial\rho/\partial z$ are neglected, and a truly local measure may take these into account, however, again, these are approximate indicators of a state which in detail requires the Navier–Stokes equations. Estimates of $\mathcal{G}$ and Fr_h are plotted in figure 19. The highest value of $\mathcal{G}$, for R10F8, is less than 30. Although the condition $\mathcal{G} > 1$ is met, recall that $\mathcal{G}$ represents the range of scales between an Ozmidov scale l_O and a Kolmogorov scale, l_K, and their ratio, $l_O/l_K \sim \mathcal{G}^{4/3}$ (de Bruyn Kops & Riley 2019). The small range of scales implied by $\mathcal{G} \leq 30$ is not
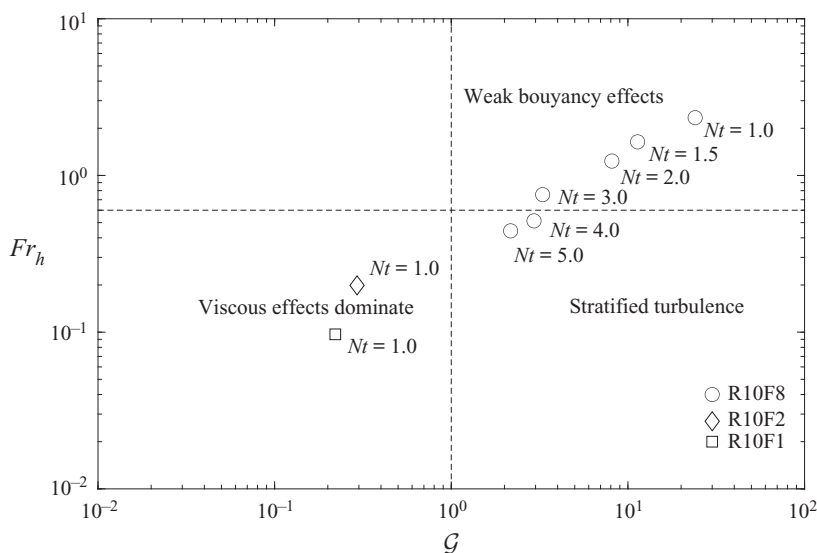
Figure 19. Plot Regime diagram, Fr_h vs $\mathcal{G}$ for $R10$ wakes. The $F1$ and $F2$ wakes immediately start in the viscous dissipation regime.

sufficient for turbulent dynamics to exist or be sustainable. Two lower Fr cases are also plotted for the earliest Nt available, and even ignoring the dubious calculation assumptions at these low $\{Re-Fr\}$, the data lie firmly in the viscous-dominated regime, as they ought. Chongsiripinyo & Sarkar (2020) constructed a similar plot, albeit for a disk wake, and with $\mathcal{R}$ on the abscissa. The initial condition of $Re = 5 \times 10^4$ allowed a starting point in weak buoyancy effects which then transitioned through all stages, WST–IST–SST, before significant viscous damping.

4. Discussion and conclusions

This work presents the first quantitative and systematic study through independent variations of Re and Fr of the canonical stratified sphere wake problem. It focuses on the domain of moderate values of both parameters ($Re \in [200, 1000]$, $Fr \in [0.5, 8]$) where the competing influences of inertial, buoyancy and viscous terms result in a number of qualitatively different flow regimes. The $\{Re-Fr\}$ parameter space is covered equally for experiments and simulations. By design it also overlaps with certain cases in OR15, and the $R10F1$ comparisons are shown in figure 20(*a*). When $Fr = 1$, the lee waves have their strongest influence on the near wake, and there is reasonable agreement up to $x/D = 5$. After that, the OR15 values are greater. Figure 20(*b*), for $R10F4$, shows that the differences may be caused at least in part by numerical resolution, as the higher resolution results agree much more closely at large x/D. Figure 20(*a*) also includes the equivalent result from Pal *et al.* (2017) which comes from a significantly higher Re run.

The reasonable agreements between experiment and simulation here are not completely trivial, since the early wake length and velocity scales depend on details of the separation location. Nevertheless, we would not advocate pushing these second-order methods to higher Re, as significantly more sophisticated numerical methods are required (e.g. Pal *et al.* 2017; de Bruyn Kops & Riley 2019; Zhou & Diamessis 2019) to deal with complex boundaries and/or initial high Re turbulence over a range of scales. One should also note that extension to lower Fr also requires significant resolution to resolve the fine structures
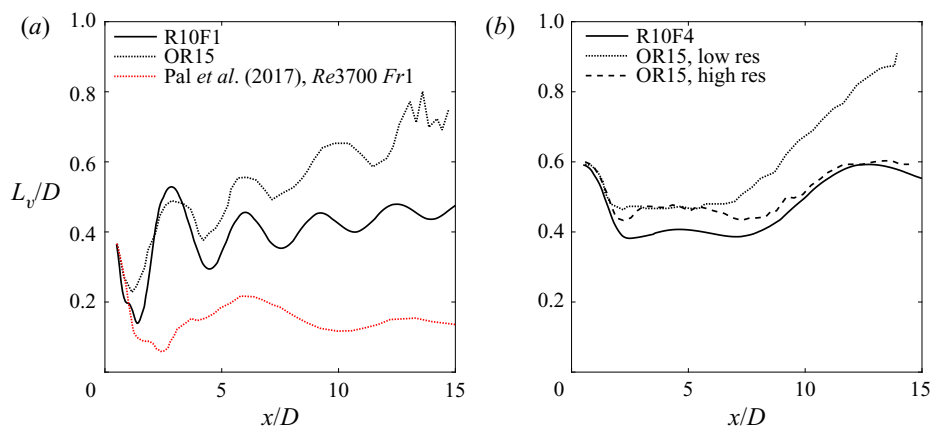
Figure 20. Vertical length scale for (*a*) *R*10*F*1 simulations, OR15 and Pal *et al.* (2017) and (*b*) *R*10*F*4, OR15 low and high resolutions. Experiments excluded for clarity, as they have been shown to be similar to simulations in the present study.

that re-emerge when $Fr < 0.5$ (Pal *et al.* 2016; Chongsiripinyo *et al.* 2017), the lowest *Fr* covered here. Both simulations and experiments will aim to explore higher *Re* domains, and existing work on the importance of the activity parameter denoted here $\mathcal{G}$ will be helpful in understanding the location in turbulence–buoyancy interactions.

Declaration of interests. The authors report no conflict of interest.

Author ORCIDs.
 T.J. Madison https://orcid.org/0000-0003-1289-7401;
 G.R. Spedding https://orcid.org/0000-0003-3033-7897.

Appendix A. Checking the numerical simulations

Early experiments and simulations have investigated the unstratified wake behind a sphere for $Re \leq 1000$ (e.g. Achenbach 1974; Tomboulides & Orszag 2000), and results from current simulations are compared in figures 21 and 22.

The streamlines are shown in figure 21 for unstratified flow in simulations. The wake at $Re = 200$ is axisymmetric, and has a recirculation region of length $1.4D$. At $Re = 300$, with weak initial perturbation, the wake cannot maintain axisymmetry, but oscillates at $St = fD/U = 0.133$ in one plane, where f is the oscillating frequency, while keeping planar symmetry in the other plane. The plane in which the wake oscillates depends on the initial perturbation. The spiral mode forms at $Re = 500$ and, in a convective time window of 250, a dual-frequency oscillation at $St = 0.168$ and $St = 0.044$ is recorded. The wake becomes more irregular at $Re = 1000$. A lower frequency is found at $St = 0.191$, and another higher frequency around 0.33, but of lower amplitude than the lower-frequency peak. The structural transitions as a function of *Re* were analysed in some detail in Tomboulides & Orszag (2000), and the symmetry breaking sequence in figure 21 is in agreement. The steady and unsteady separation sequence leads to variations in C_D and *St*, which are compared with literature values in figure 22. The agreement is satisfactory for the integrated force measure of C_D and for *St*, including the simultaneous presence of high and low modes.
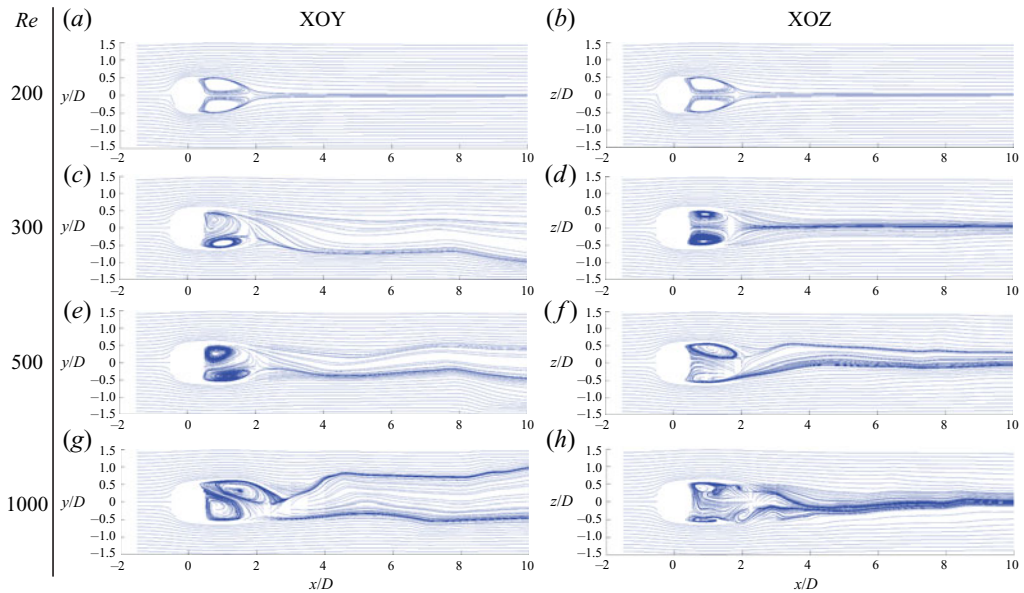
Figure 21. Streamline projections onto horizontal (*a,c,e,g*) and vertical (*b,d,f,h*) planes for the unstratified flow past a sphere.
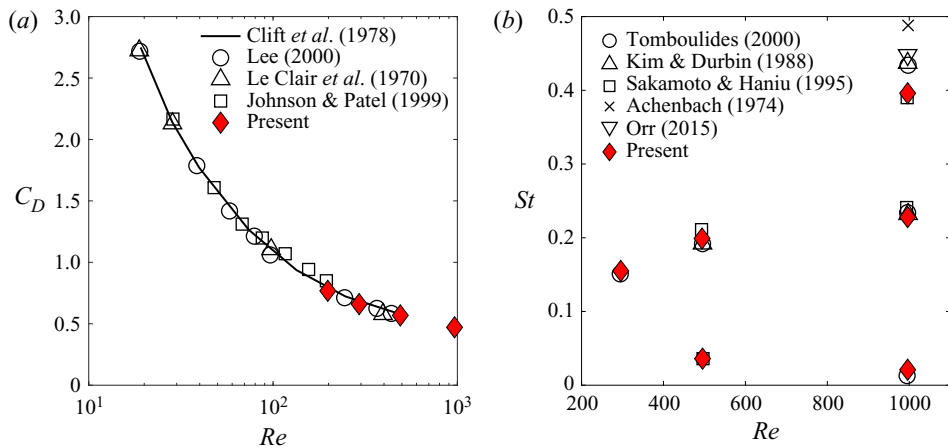

Figure 22. Estimates of drag coefficient and Strouhal number for unstratified sphere wakes.

Finite volume methods yield numerically induced wave dispersion errors (cf. Fletcher 1991) where wave propagation angles and speeds vary with frequency/wavenumber. The magnitude of these errors depends on the wavelength, λ, in the flow compared with the mesh size, Δ, and can be estimated both *a priori* and *a posteriori* for certain configurations (including multidimensional, nonlinear flows) (Schranner *et al.* 2015; Castiglioni, Sun & Domaradzki 2019) but accurate estimates are difficult for 3-D flows on unstructured meshes, and one strives for large λ/Δ, The internal waves that we may claim to simulate have $\lambda = O(D)$, and dispersion errors will be small when $\lambda/\Delta \approx 0.025$. Internal waves propagate from their source and then the selection of appropriate far-field boundary conditions also becomes more critical. The selection of boundary conditions for the finite
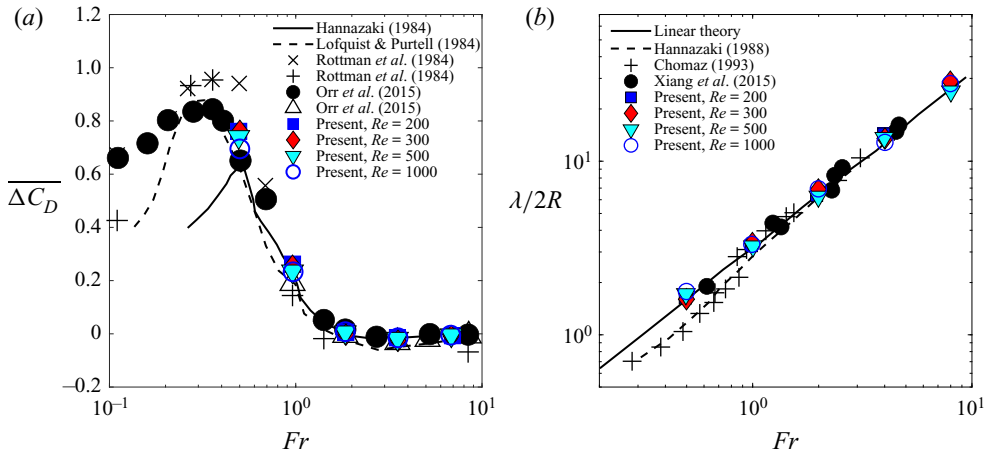
933 A12-24

Figure 23. (*a*) The change in time-averaged drag coefficient at varying *Fr* for a range of experiments and simulations (modified from Orr *et al.* 2015); (*b*) lee wavelengths immediately behind the sphere closely match the $\lambda = 2\pi R.Fr$ prediction.

volume solvers in OpenFOAM is described in some detail in Chen & Spedding (2017), which also describes the generation of the expected St Andrew's cross internal waves in response to periodic pointwise forcing in the domain centre. For $\omega/N = \sqrt{3}/2, \sqrt{2}/2$ and $1/2$, the angle of the isophase lines from the vertical, θ, were not significantly different from predicted values (Lighthill 1978; Voisin 1991) of $\theta = \pi/6$, $\pi/4$ and $\pi/3$.

At low *Fr*, the near wake is strongly influenced by the lee wave of the sphere and denoting

$$\overline{\Delta C_D} = C_D(Re, Fr) - C_D(Re, \infty) \tag{A1}$$

the difference in drag coefficient for varying *Fr* is plotted in figure 23(*a*). In the range $0.5 \leq Fr \leq 8$ there is reasonable agreement between experiment and simulations (these and from Rottman *et al.* 2010; Orr *et al.* 2015). Below $Fr = 0.5$ there is considerable variation and Pal *et al.* (2016) have shown how small-scale fluctuations re-appear at very low *Fr*, requiring once again very fine grid resolution.

The wavelength, $\lambda/2R$ of linear internal waves is $\pi.Fr$, and matches well with observations here and in the literature, both for spheres (Hanazaki 1988; Chomaz *et al.* 1993) and even quite well for circular cross-section grids (Xiang *et al.* 2015). At $Fr \geq 1$, Voisin (2007) invokes U/N as a scale for outer regions influenced by low-amplitude oscillations in the inner wake and from table 1, for case R10F8, $U/(2\pi N) \approx 1.7$ cm which is close to the physical sphere diameter. Low-amplitude wake oscillations that generate internal waves ought therefore to be accommodated in the numerical scheme, but we cannot make a general claim about turbulence-generated, small-scale waves.

REFERENCES

ABDILGHANIE, A.M. & DIAMESSIS, P.J. 2013 The internal gravity wave field emitted by a stably stratified turbulent wake. *J. Fluid Mech.* **720**, 104–139.

ACHENBACH, E. 1974 Vortex shedding from spheres. *J. Fluid Mech.* **62**, 209–221.

BEVILAQUA, P.M. & LYKOUDIS, P.S. 1978 Turbulence memory in self-preserving wakes. *J. Fluid Mech.* **89**, 589–606.

BILLANT, P. & CHOMAZ, J.M. 2001 Self-similarity of strongly stratified inviscid flows. *Phys. Fluids* **13** (6), 1645–1651.

BONNIER, M. & EIFF, O. 2002 Experimental investigation of the collapse of a turbulent wake in a stably stratified fluid. *Phys. Fluids* **14** (2), 791–801.

BRETHOUWER, G., BILLANT, P., LINDBORG, E. & CHOMAZ, J.M. 2007 Scaling analysis and simulation of strongly stratified turbulent flows. *J. Fluid Mech.* **585**, 343–368.

BRUCKER, K.A. & SARKAR, S. 2010 A comparative study of self-propelled and towed wakes in a stratified fluid. *J. Fluid Mech.* **652**, 373–404.

DE BRUYN KOPS, S. & RILEY, J. 2019 The effects of stable stratifiecation on the decay of initially isotropic homogenous tubulence. *J. Fluid Mech.* **860**, 787–821.

CASTIGLIONI, G., SUN, G. & DOMARADZKI, J.A. 2019 On the estimation of artificial dissipation and dispersion errors in a generic partial differential equation. *J. Comput. Phys.* **397**, 108843.

CHEN, K.K. & SPEDDING, G.R. 2017 Boussinesq global modes and stability sensitivity, with applications to stratified wakes. *J. Fluid Mech.* **812**, 1146–1188.

CHOMAZ, J.-M., BONETTON, P., BUTET, A. & HOPFINGER, E.J. 1993 Vertical diffusion of the far wake of a sphere moving in a stratified fluid. *Phys. Fluids* **5** (11), 2799–2806.

CHONGSIRIPINYO, K., PAL, A. & SARKAR, S. 2017 On the vortex dynamics of flow past a sphere in $Re = 3700$ in a uniformly stratified fluid. *Phys. Fluids* **29**, 020703.

CHONGSIRIPINYO, K. & SARKAR, S. 2020 Decay of turbulent wakes behind a disk in homogeneous and stratified fluids. *J. Fluid Mech.* **885**, A31.

CLIFT, R., GRACE, J.R. & WEBER, M.E. 1978 *Bubbles Drops and Particles*. Academic Press.

DIAMESSIS, P.J., GURKA, R. & LIBERZON, A. 2010 Spatial characterization of vortical structures and internal waves in a stratified turbulent wake using proper orthogonal decomposition. *Phys. Fluids* **22**, 086601.

DIAMESSIS, P.J., SPEDDING, G.R. & DOMARADZKI, J.A. 2011 Similarity scaling and vorticity structure in high-Reynolds-number stably stratified turbulent wakes. *J. Fluid Mech.* **671**, 52–95.

DOMMERMUTH, D.G., ROTTMAN, J.W., INNIS, G.E. & NOVIKOV, E.A. 2002 Numerical simulation of the wake of a towed sphere in a weakly stratified fluid. *J. Fluid Mech.* **473**, 83–101.

FLETCHER, C.A.J. 1991 *Computational Techniques for Fluid Dynamics*, vol. 1. Springer.

GARGETT, A., OSBORN, T. & NASMYTH, P 1984 Local isotropy and the decay of turbulence in a stratified fluid. *J. Fluid Mech.* **144**, 231–280.

GEORGE, W.K. 1989 The self-preservation of turbulent flows and its relation to initial conditions and coherent structures. In *Advances in Turbulence* (ed. W.K. George & R.E.A. Arndt), pp. 39–73. Hemisphere.

GIBSON, C.H. 1980 Fossil temperature, salinity and vorticity in the ocean. In *Marine Turbulence* (ed. J.C.T. Nihoul), pp. 221–258. Springer.

GIBSON, C.H, CHEN, C.C & LIN, S.C 1968 Measurements of turbulent velocity and temperature fluctuations in the wake of a sphere. *AIAA J.* **6**, 642–649.

GODOY-DIANA, R., CHOMAZ, J.-M. & BILLANT, P. 2004 Vertical length scale selection for pancake vortices in strongly stratified viscous fluids. *J. Fluid Mech.* **504**, 229–238.

GOURLAY, M.J., ARENDT, S.C., FRITTS, D.C. & WERNE, J. 2001 Numerical modeling of initially turbulent wakes with net momentum. *Phys. Fluids* **13**, 3783–3802.

HANAZAKI, H. 1988 A numerical study of three-dimensional stratified flow past a sphere. *J. Fluid Mech.* **192**, 393–419.

JOHNSON, T.A. & PATEL, V.C. 1999 Flow past a sphere up to a Reynolds number of 300. *J. Fluid Mech.* **378**, 19–70.

KIM, H.J. & DURBIN, P.A. 1988 Observations of the frequencies in a sphere wake and of drag increase by acoustic excitation. *Phys. Fluids* **31**, 3260–3265.

LE CLAIR, B.P., HAMIELEC, A.E. & PRUPPACHER, H.R. 1970 A numerical study of the drag on a sphere at low and intermediate Reynolds numbers. *J. Atmos. Sci.* **27**, 308–315.

LEE, S. 2000 A numerical study of the unsteady wake behind a sphere in a uniform flow at moderate Reynolds numbers. *Comput. Fluids* **29**, 639–667.

LIGHTHILL, M.J. 1978 *Waves in Fluids*. Cambridge University Press.

LIN, Q., BOYER, D.L. & FERNANDO, H.J.S. 1992 Turbulent wakes of linearly stratified flow past a sphere. *Phys. Fluids* **4** (8), 1687–1696.

LINDBORG, E. 2006 The energy cascade in a strongly stratified fluid. *J. Fluid Mech.* **550**, 207–242.

LOFQUIST, K.E. & PURTELL, L.P. 1984 Drag on a sphere moving horizontally through a stratified liquid. *J. Fluid Mech.* **148**, 271–284.

MAGNAUDET, J., RIVERO, M. & FABRE, J. 1995 Accelerated flows past a rigid sphere or a spherical bubble. Part 1. Steady straing flow. *J. Fluid Mech.* **284**, 97–135.

MÉTAIS, O. & HERRING, J.R. 1989 Numerical simulations of freely evolving turbulence in stably stratified fluids. *J. Fluid Mech.* **202**, 117–148.

MEUNIER, P., DIAMESSIS, P.J. & SPEDDING, G.R. 2006 Self-preservation in stratified momentum wakes. *Phys. Fluids* **18**, 106601.

MEUNIER, P., LE DIZES, S., REDEKOPP, L.G. & SPEDDING, G.R. 2018 Internal waves generated by a stratified wake: experiment and theory. *J. Fluid Mech.* **846**, 752–788.

MEUNIER, P. & SPEDDING, G.R. 2004 A loss of memory in stratified momentum wakes. *Phys. Fluids* **16**, 298–303.

MEUNIER, P. & SPEDDING, G.R. 2006 Stratified propelled wakes. *J. Fluid Mech.* **552**, 229–256.

NASTROM, G.D. & GAGE, K.S. 1985 A climatology of atmospheric wavenumber spectra of wind and temperature observed by commercial aircraft. *J. Atmos. Sci.* **42**, 950–960.

NASTROM, G.D., GAGE, K.S. & JASPERSON, W.H. 1984 Kinetic energy spectrum of large- and mesoscale atmospheric processes. *Nature* **310**, 36–38.

NAYAR, K.G., SHARQAWY, M.H., BANCHIK, L.D. & LIENHARD, J.H. 2016 Thermophysical properties of seawater: a review and new correlations that include pressure dependence. *Desalin. Water Treat.* **390**, 1–24.

ORR, T.S., DOMARADZKI, J.A., SPEDDING, G.R. & CONSTANTINESCU, G.S. 2015 Numerical simulations of the near wake of a sphere moving in a steady, horizontal motion through a linearly stratified fluid at *Re* = 1000. *Phys. Fluids* **27** (3), 035113.

ORTIZ-TARIN, J.L., CHONGSIRIPINYO, K.C. & SARKAR, S. 2019 Stratified flow past a prolate spheroid. *Phys. Rev. Fluids* **4**, 094803.

PAL, A., SARKAR, S., POSA, A. & BALARAS, E. 2016 Regeneration of turbulent fluctuations in low-Froude-number flow over a sphere at a Reynolds number of 3700. *J. Fluid Mech.* **804**, R2.

PAL, A., SARKAR, S., POSA, A. & BALARAS, E. 2017 Direct numerical simulation of stratified flow past a sphere at subcritical Reynolds number of 3700 and moderate Froude number. *J. Fluid Mech.* **826**, 5–31.

REDFORD, J.A., CASTRO, I.P. & COLEMAN, G.N. 2012 On the universality of turbulent axisymmetric wakes. *J. Fluid Mech.* **710**, 419–452.

REDFORD, J.A., LUND, T.S. & COLEMAN, G.N. 2015 A numerical study of a weakly stratified turbulent wake. *J. Fluid Mech.* **776**, 568–609.

RILEY, J.J. & DE BRUYN KOPS, S.M. 2003 Dynamics of turbulence strongly influenced by buoyancy. *Phys. Fluids* **15**, 2047–2059.

ROTTMAN, J.W., BRUCKER, K.A., DOMMERMUTH, D.G. & BROUTMAN, D. 2010 Parameterization of the near-field internal wave field generated by a submarine. In *Proc. 28th Symp. on Naval Hydrodynamics*, p. 790. Office of Naval Research.

ROWE, K.L., DIAMESSIS, P.J. & ZHOU, Q 2020 Internal gravity wave radiation from a stratified turbulent wake. *J. Fluid Mech.* **888**, A25.

SAKAMOTO, H. & HANUI, H. 1995 The formation mechanism and shedding frequency of vortices from a sphere in uniform shear flow. *J. Fluid Mech.* **287**, 151–171.

SCHRANNER, F., DOMARADZKI, J.A., HICKEL, S. & ADAMS, N. 2015 Assessing the numerical dissipation rate and viscosity in numerical simulation of fluid flows. *Comp. Fluids* **114**, 84–97.

SPEDDING, G.R. 1997 The evolution of initially turbulent bluff-body wakes at high internal Froude number. *J. Fluid Mech.* **337**, 283–301.

SPEDDING, G.R. 2001 Anisotropy in turbulence profiles of stratified wakes. *Phys. Fluids* **13** (8), 2361–2372.

SPEDDING, G.R. 2002 Vertical structure in stratified wakes with high initial Froude number. *J. Fluid Mech.* **454**, 71–112.

SPEDDING, G.R., BROWAND, F.K. & FINCHAM, A.M. 1996*a* The long-time evolution of the initially turbulent wake of a sphere in a stable stratification. *Dyn. Atmos. Ocean.* **23**, 171–182.

SPEDDING, G.R., BROWAND, F.K. & FINCHAM, A.M. 1996*b* Turbulence, similarity scaling and vortex geometry in the wake of a towed sphere in a stably stratified fluid. *J. Fluid Mech.* **314**, 53–103.

TOMBOULIDES, A.G. & ORSZAG, S.A. 2000 Numerical investigation of transitional and weak turbulent flow past a sphere. *J. Fluid Mech.* **416**, 45–73.

TOWNSEND, A.A. 1976 *The Structure of Turbulent Shear Flow*, 2nd edn. Cambridge University Press.

UBEROI, M.S. & FREYMUTH, P. 1970 Turbulent energy balance and spectra of the axisymmetric wake. *Phys. Fluids* **13** (9), 2205–2210.

VOISIN, B. 1991 Internal wave generation in uniformly stratified fluids. Part 1. Green's function and point sources. *J. Fluid Mech.* **231**, 439–480.

VOISIN, B. 2007 Lee waves from a sphere in a stratified flow. *J. Fluid Mech.* **574**, 273–315.

WATANABE, T., RILEY, J.J., DE BRUYN KOPS, S.M., DIAMESSIS, P.J. & ZHOU, Q. 2016 Turbulent/non-turbulent interfaces in wakes in stably stratified fluids. *J. Fluid Mech.* **797**, R1.

XIANG, X., MADISON, T.J., SELLAPPAN, P. & SPEDDING, G.R. 2015 The turbulent wake of a towed grid in a stratified fluid. *J. Fluid Mech.* **775**, 149–177.

ZHOU, Q. & DIAMESSIS, P.J. 2019 Large-scale characteristics of stratified wake turbulence at varying Reynolds number. *Phys. Rev. Fluids* **4**, 084802.